

# Geometry and dynamics of an East Antarctic Ice Sheet outlet glacier, under past and present climates

N. R. Golledge<sup>1</sup> and R. H. Levy<sup>2</sup>

Received 11 March 2011; revised 26 May 2011; accepted 6 July 2011; published 28 September 2011.

[1] The behavior of East Antarctic Ice Sheet (EAIS) outlet glaciers both at present and during the recent geological past is of considerable interest both from the point of view of understanding the mechanics of contemporary glacier dynamics, and also with regard to epoch-scale ice sheet stability during Plio-Pleistocene climate transitions. Here we use a glacier flowline model that incorporates the effects of longitudinal stresses to numerically simulate Ferrar Glacier, first under present-day environmental conditions, and subsequently under both colder and warmer climate regimes representing the Last Glacial Maximum (LGM) and mid-Pliocene peak warmth respectively. Using airborne radar profiles, InSAR-derived surface velocities, ice core and geological data for empirical constraint, we present a diagnostic simulation that uses an iterative method to closely reproduce observed dynamics. Our model suggests that the glacier is largely cold-based under present conditions, flows predominantly by way of internal deformation, and ‘cascades’ over bedrock ridges due to the combined action of changes in cross-sectional valley geometry, local steepening of the glacier surface, and the non-local effects of longitudinal coupling. Time-dependent (evolutionary) simulation of a lower-profile glacier under a colder, drier, LGM climate, predicts flow velocities lower than present with minimal bedrock erosion or basal till flux. Conversely, the warmer-than-present mid-Pliocene climate produces a more dynamic glacier that is warm-based and sliding along much of its bed. We propose that EAIS outlet glaciers, such as the Ferrar, respond dynamically along their length in response to changing environmental forcings, with most significant changes taking place in their lower reaches. Adjustment to perturbations in upper catchments is more muted.

**Citation:** Golledge, N. R., and R. H. Levy (2011), Geometry and dynamics of an East Antarctic Ice Sheet outlet glacier, under past and present climates, *J. Geophys. Res.*, 116, F03025, doi:10.1029/2011JF002028.

## 1. Introduction

[2] In this paper we describe the numerics of a one-dimensional ice sheet flowline model and its application to Ferrar Glacier, East Antarctica. We have two aims. The first is to present a diagnostic simulation of Ferrar Glacier, constrained by present climatic and topographic boundary conditions, in order to provide a new assessment of the glacier’s present-day behavior, since previous studies of Ferrar and neighboring Taylor Glacier have led to conflicting views regarding the fundamental mechanism of flow of these outlets [cf. *Johnson and Staiger*, 2007; *Kavanaugh et al.*, 2009a]. The second goal is to use our model to investigate the likely dynamical behavior of Ferrar Glacier, and changes in its steady state geometry, during colder (Last Glacial Maximum - LGM, c. 21 ka BP) and warmer (mid-Pliocene,

c. 3–4 Ma BP) geological periods. Our model accounts for the dynamical effects exerted by longitudinal stresses, and uses flow parameters tuned during the diagnostic simulation to reproduce InSAR-derived glacier centerline velocities as closely as possible. This is achieved by way of an iterative procedure in which the glacier surface is held fixed but the bed topography is incrementally modified during the integration until mismatch between observed and modeled velocities is reduced. Subsequent time-dependent simulations under colder and warmer paleoclimate scenarios use the ice thickness distribution and iterated bed profile calculated in the diagnostic run to investigate likely LGM and warm Pliocene glacier characteristics, in the anticipation that such insights might be pertinent to the long-standing debate concerning the epoch-scale stability of the East Antarctic Ice Sheet (EAIS) [*Webb et al.*, 1984; *Sugden et al.*, 1993; *Wilson*, 1995; *Siegert et al.*, 2008], and be of wider relevance in considering possible responses of transantarctic glaciers to observed continental-scale changes highlighted in recent studies [e.g., *Chen et al.*, 2009; *Pritchard et al.*, 2009; *Steig et al.*, 2009]. Our model also incorporates components that enable a qualitative exploration of the influence exerted by

<sup>1</sup>Antarctic Research Centre, Victoria University of Wellington, Wellington, New Zealand.

<sup>2</sup>GNS Science, Lower Hutt, New Zealand.

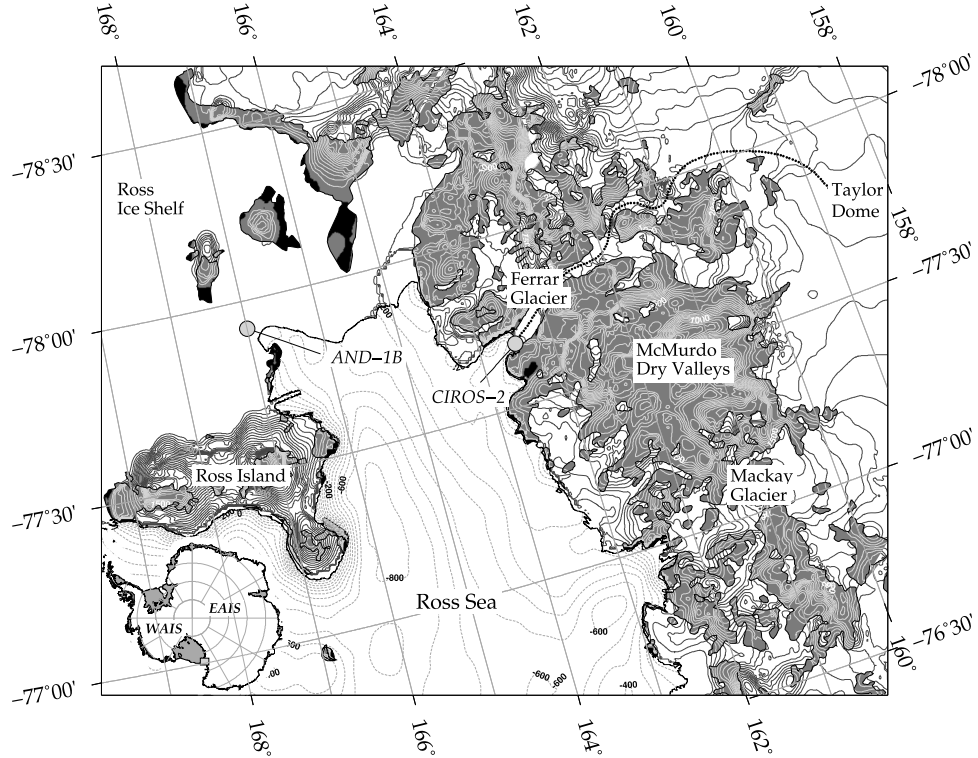


**Figure 1.** Ferrar Glacier and surrounding area, based on 1 km ERS-1 and ICESat topographic data [Bamber *et al.*, 2009], and MAMM 25 m coastline [Liu and Jezek, 2004], clipped according to areas of exposed rock (Antarctic Digital Database, <http://www.add.scar.org/>). Bathymetric contours interpolated from ALBMAPv1 topographic data [Le Brocq *et al.*, 2010]. Path of radar echo profile [Calkin, 1974] shown with dotted line; major geological drill sites marked with circles.

thermal regime on subglacial substrate evolution. In doing so we are able to identify first-order differences in the likely geological signature of Ferrar Glacier under each of the three contrasting climatic scenarios (LGM, Present, mid-Pliocene). This is relevant in the context of previous geological studies, which have mapped glacial limits [Denton *et al.*, 1989, 1993; Marchant *et al.*, 1993; Wilch *et al.*, 1993; Denton and Hughes, 2000], interpreted sedimentary sequences recovered by drilling [McKelvey, 1981, 1982; Pyne *et al.*, 1985; Barrett and Hambrey, 1992; Ishman and Rieck, 1992], and inferred glaciological characteristics of outlets in this area [Staiger *et al.*, 2006].

## 2. Model Domain

[3] Ferrar Glacier provides a southern bound to the largely ice-free area of the McMurdo Dry Valleys, Victoria Land, draining ice from the summit of Taylor Dome ( $77^{\circ}47'47''S$ ,  $158^{\circ}43'26''E$ , 2365 m) [Morse *et al.*, 1999] through the Transantarctic Mountains to a grounding line 290 m below present sea level in the Ross Sea (Figure 1). The glacier's junction with this embayment of the Southern Ocean is defined by a short (c. 15 km) floating ice tongue whose surface lies 24 m above present sea level [Calkin, 1974]. From Taylor Dome to present tidewater terminus, the sinuous drainage route of Ferrar Glacier is approximately 142 km in length. Surface slopes in the plateau area of the upper Ferrar are around  $7.9 \text{ m km}^{-1}$ , whereas the average gradient of the glacier descending from the plateau margin

to the present grounding line is approximately  $25.8 \text{ m km}^{-1}$ . Valley widths range from  $>10 \text{ km}$  to  $<2 \text{ km}$ . Ice thickness around Taylor Dome is  $\approx 800 \text{ m}$ , in the upper Ferrar  $\approx 1000 \text{ m}$ , and in the outlet glacier  $\approx 500 \text{ m}$  (Figure 2). Considerable down-glacier deviation from these order-of-magnitude figures is evident in a radio echo profile of the bed [Calkin, 1974], which reveals both  $\approx 10 \text{ km}$  wavelength bedrock undulations with amplitudes of hundreds of meters, and higher-frequency, lower amplitude relief (Figure 3).

## 3. Input Data and Modeling Strategy

### 3.1. Glaciological and Topographic Data

[4] A topographic and ice thickness radar profile of Ferrar Glacier obtained during the 1970's [Calkin, 1974], is used to initialize our flowline model. On the basis of discrepancies on neighboring Taylor Glacier between ground-based GPR measurements and Calkin's profile, however, Kavanaugh *et al.* [2009a] question whether the Calkin data set accurately captures the bed topography of Ferrar Glacier centerline. They note an underestimate of ice thickness in the Calkin [1974] Taylor Glacier profile, possibly due to 'side reflections and wanderings of the flight path', and postulate that this may have been one of the sources of error that led to the 'problematic' [Kavanaugh *et al.*, 2009a, p. 10] model of Ferrar Glacier flow proposed by Johnson and Staiger [2007]. Given that newer ice thickness data are only available for a very limited section of Ferrar Glacier, we attempt to improve our simulation in two ways. Firstly, we implement

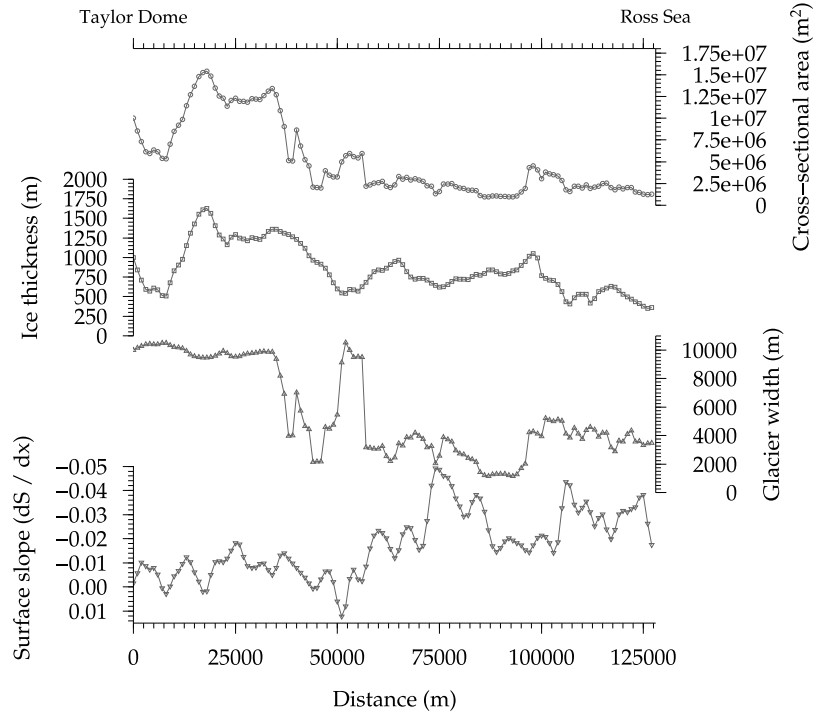


**Figure 2.** Variability in glacier geometry in the model domain. Surface slopes calculated as first derivative of Calkin [1974] surface elevations, widths based on cross-valley extent of main glacier (ignoring tributaries), thickness and cross-sectional area derived from iterative procedure described in text.

an inverse procedure in order to recover a likely bed profile, which we subsequently use for both diagnostic and time-dependent simulations. Our iterative method takes as input InSAR-derived velocity values [Kavanaugh *et al.*, 2009a], in which data gaps are filled using a standard cubic spline. Secondly, we incorporate a width term into our flux calculations, such that the accelerating effects of valley narrowings are better accounted for than in the Johnson and Staiger [2007] model.

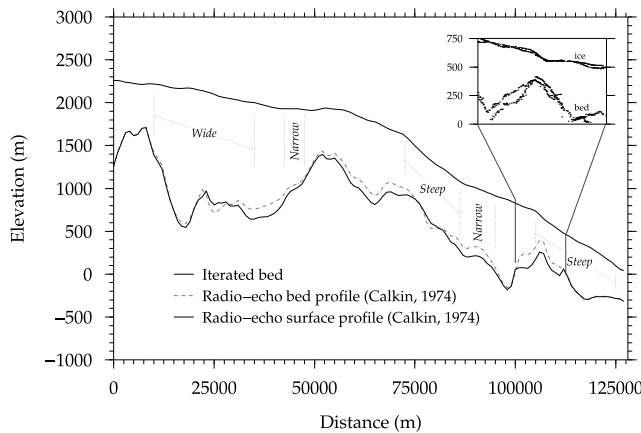


**Figure 3.** Glacier surface and bed elevations from this study and that of the radio echo profile of Calkin [1974]. Iterated bed profile simulated in this study based on the procedure described in the text. Inset shows unprocessed ice surface and bed returns from 2009 radar survey (D. Young, personal communication, 2010).

### 3.2. Climatic Forcing and Boundary Conditions

[5] Model experiments are forced with climatic parameterizations (Table 1) that incorporate regional inferences from gridded data sets as well as an empirically derived elevation–ablation rate function calculated for neighboring Taylor Glacier [Bliss *et al.*, 2011]. Time-dependent simulations are run for 10000 model years each. Relative sea level elevation and near-surface ocean temperature for present-day are based on observational data [Orsi and Whitworth, 2004]. Glaciological parameters such as the flow law exponent, as well as those related to the physical properties of ice, are held constant at commonly used values obtained from the literature (Table 2). We prescribe a boundary condition of zero ice flux at the top of the domain.

### 3.3. Modeling Strategy

#### 3.3.1. Diagnostic Simulation

[6] In order to address our principal aim of investigating the present-day behavior of Ferrar Glacier, we first seek to generate a diagnostic solution to the mass conservation equations that replicates as closely as possible the present-day glacier velocity profile as interpreted from InSAR data [Kavanaugh *et al.*, 2009a]. This is achieved using a two stage approach. First, we hold ice surface elevation and bed topography constant and run a one-year model integration. The procedure is repeated, making systematic adjustments to sliding rate and deformation enhancement factors, until the surface velocity solution approaches that described by the InSAR data. This approximation of the velocity distribution is then refined by implementing a second technique, in which ice surface elevations, sliding and deformation parameters are held fixed, and bed elevation is incrementally

**Table 1.** Environmental Bounding Conditions

	Present	LGM	Mid-Pliocene	Source
Relative sea level (m)	0	+50	+25	Peltier [2004]; Dwyer and Chandler [2009]
Sea surface temperature ( $T_s$ , °C)	-1.6	-1.8	0.5	tuning parameter
Calving rate coefficient ( $\eta$ )	0.125	0.02	0.95	tuning parameter
MAT at sea level (°C)	-17	-20	-7	Comiso [1994]; Johnson and Staiger [2007]
Precip. at sea level (ma <sup>-1</sup> )	0.19	0.19	0.38	Morse et al. [1999]; Vaughan et al. [1999]
Annual temp. range (°C)	25	25	25	estimated, cf. Bliss et al. [2011]
Temp. lapse rate (K km <sup>-1</sup> )	$-1.053 \times 10^1$	$-1.053 \times 10^1$	$-1.053 \times 10^1$	Morse et al. [1999]
Precip. lapse rate (ma <sup>-1</sup> km <sup>-1</sup> )	$-5.05 \times 10^{-2}$	$-1.01 \times 10^{-1}$	$-5.05 \times 10^{-2}$	Vaughan et al. [1999]; Monnin et al. [2004]

adjusted if  $|U_{mod(x,t)} - U_{obs(x,t)}| > \Gamma$ , in which the left-hand side defines the mismatch between modeled and observed velocities at each point  $x$  and time  $t$ , and  $\Gamma$  denotes a prescribed tolerance. Bed elevation for the subsequent iteration is then given by:

$$b(x) = S(x) - \left( H(x) + \left( \min \left[ \frac{(U_{mod(x)} - U_{obs(x)})}{\varphi}, \Psi \right] \right) \right) \quad (1)$$

where the denominator  $\varphi$  and upper bound  $\Psi$  control the magnitude of each adjustment.

[7] We iterate through this procedure until modeled ice velocities produce as close a visual match to observed values as possible. The value of  $\Gamma$  ( $= 2.5 \text{ m a}^{-1}$ ) was determined through experimentation in a manner intended to balance mismatch minimization against possible over-fitting. Although this scheme lacks the rigor of two-dimensional control method inversions [e.g., MacAyeal, 1993; Vieli and Payne, 2003; Jougin et al., 2004], it benefits from an ease of implementation, and is considered adequate for the one-dimensional nature of our problem.

### 3.3.2. Time-Dependent Simulations

[8] We adopt the iterated present-day ice thickness distribution as initializing data for our time-dependent simulations of Ferrar Glacier dynamics under colder (LGM) and warmer (mid-Pliocene) climatic conditions. We use inferences from the Taylor Dome ice core [Morse et al., 1999] and from cosmogenic surface exposure dating [Staiger

et al., 2006] to guide our parameterization of ice thickness under LGM and mid-Pliocene conditions at the head of our domain respectively, and, in order to tune as few parameters as possible, we modify only climatic (sea level temperature, sea level precipitation, precipitation lapse rate) and oceanic variables (sea level elevation, ocean temperature, calving rate). Some of these are relatively well-constrained by local empirical evidence, but others require inference from modeling, or from regional geological and paleoenvironmental sources. Our parameterization of climatic components uses values adopted by Staiger et al. [2006] and Johnson and Staiger [2007] (Table 1); LGM relative sea level elevation (+50 m) is based on results of a global isostatic model [Peltier, 2004], and mid-Pliocene values are based on geological data indicating a eustatic sea level also slightly higher than present (c. +25 m) [Wardlaw and Quinn, 1991; Naish, 1997; Naish et al., 2005; Dwyer and Chandler, 2009]. Ocean temperatures and calving rate are unknown quantities for all paleo scenarios, and therefore require further consideration. Geological evidence indicates a thick, grounded, ice sheet in the Ross Sea at LGM that would have precluded oceanic interaction with the Ferrar glacier terminus [Denton et al., 1989; Conway et al., 1999; Denton and Hughes, 2000], despite higher relative sea levels [Peltier, 2004], thus the influence exerted by ocean temperatures is taken to be nil and regulation of ice thickness at the present grounding line location is assumed to have occurred only via flux into the grounded ice sheet in the now Ross Sea. Incremental reduction of our imposed calving scalar (as a proxy for the flux described above) from values of our present-day scenario allows us to reproduce an ice surface elevation increase at the present-day grounding line location that is very close to the  $\approx 400 \text{ m}$  thickening inferred from geological reconstructions [Denton and Marchant, 2000]. Geological data preserved in the CIROS-2 drill core reveal multiple cycles of advance and retreat of the Ferrar Glacier in the warm mid-Pliocene [Barrett and Hambrey, 1992]. Massive diamictite intervals indicate that grounded ice advanced across the drill site during peak glacial periods. However, distinct diatom-rich mudstone intervals reflect phases of maximum ice margin retreat, during which a seasonally sea-ice-free open marine embayment occupied Ferrar Fjord [Winter, 1995; Winter and Harwood, 1997]. Furthermore, data from the nearby AND-1B core (Figure 1) indicate that summer sea surface temperatures in the Ross Embayment may have been as high as  $3\text{--}5^\circ\text{C}$  during these episodes of peak Pliocene warmth [Winter et al., 2010, 2011]. Such data depict a relatively warm ocean-atmosphere environment in Ferrar Fjord during periods of the mid-Pliocene, likely leading to high calving rates (softer ice,

**Table 2.** Physical and Model Constants

Parameter	Symbol	Value	Units
Density of ice	$\rho$	920	$\text{kg m}^{-3}$
Density of seawater	$\rho_w$	1028	$\text{kg m}^{-3}$
Density of mantle	$\rho_m$	3300	$\text{kg m}^{-3}$
Gravitational acceleration	$g$	9.81	$\text{m s}^{-2}$
Sliding rate factor	$f_{s0}$	$1 \times 10^{-11}$	-
Glen's flow law exponent	$n$	3	-
Sliding exponent	$p$	3	-
Flow enhancement factor	$E$	7.5	-
Thermal parameter ( $T \geq 263.15 \text{ K}$ )	$\xi$	5.47e10	-
Thermal parameter ( $T < 263.15 \text{ K}$ )	$\xi$	1.14e-5	-
Till thickness limiting bedrock erosion	$\varphi_{max}$	2	m
Universal gas constant	$R$	8.314	$\text{J mol}^{-1} \text{ K}^{-1}$
Degree-day factor	$F_{pdd}$	0.005	$\text{m yr}^{-1}$
Geothermal heat flux	$G$	68	$\text{mW m}^{-2}$
Thermal conductivity of ice	$\kappa_{ice}$	2.4	$\text{W m}^{-1} \text{ K}^{-1}$
Lithospheric relaxation time	$\theta$	3000	yr
Calving constant	$c$	17	-
Horizontal domain resolution	$\Delta x$	1000	m
Valley-side angle	$\alpha$	45	°
Creep activation energy	$Q$	139 or 60	$\text{kJ mol}^{-1}$

higher strain rates) and enhanced submarine melt at the terminus. We impose oceanic parameters in line with these geological inferences, bringing about a retreated Ferrar Glacier whose terminus is grounded at sea level and whose mass balance is subsequently governed only by atmospheric conditions.

#### 4. Numerical Model Formulation

[9] We use a 1-dimensional finite difference flowline model to simulate ice thickness evolution at 1 km horizontal resolution, using a forward explicit numerical scheme implemented over a staggered grid that spans the grounded length of the Ferrar Glacier. The core of the flowline model is typical of many flowline models [e.g., *Oerlemans*, 1997; *Pattyn*, 2006; *De Boer et al.*, 2010], but specifically incorporates stress and mass balance equations appropriate to Transantarctic Mountain glaciers. We account for the effects of horizontal variations in valley width by calculating fluxes through a cross-sectional plane described by a symmetrical trapezoid, and by including a width-dependent shape factor that uses tabulated values for a parabolic glacier cross-profile [*Cuffey and Paterson*, 2010]. We incorporate basal sliding into our model so that dynamic behavioral contrasts between warm and cold climatic scenarios can be identified. Our model also incorporates bedrock erosion and till flux components. The model is coded in Python, using Numeric (NumPy) and Scientific (SciPy) libraries. All model constants and variables are presented in Tables 2 and 3 respectively.

[10] The rate of ice thickness change is calculated from the continuity (mass conservation) equation:

$$\frac{\partial H}{\partial t} = M - \nabla \cdot q \quad (2)$$

which represents a steady state solution when the gradient of ice flux ( $\nabla \cdot q$ ) is balanced by net accumulation ( $M$ ). In our model, this is implemented in a standard form where the change in ice thickness through time is calculated from the centerline velocity ( $u$ ) solution and symmetrical trapezoidal cross-sectional area ( $\gamma$ ), at the previous time step:

$$\frac{\partial \gamma}{\partial t} = \frac{\partial}{\partial x} (\gamma u) + M \quad (3)$$

where

$$\gamma = H^2 \tan \alpha + H w_b \quad (4)$$

in which  $\alpha$  defines the valley side angle from vertical and  $w_b$  is the valley width at the base of the glacier.

[11] The continuity equation is integrated through time using an adaptive time stepping scheme [*Hindmarsh*, 2001], based on the Courant-Friedrichs-Lowy stability criterion, in which  $dt$  is governed primarily by grid size and peak ice flux:

$$dt = \frac{(\Delta x)^2}{2n \times \max \left[ Hu \left( \frac{\partial S}{\partial x} \right)^{-1} \right]} \quad (5)$$

##### 4.1. Ice Dynamics

[12] Solving the shallow-ice approximation of the conservation of momentum equations yields a stress balance

solution that reflects the general pattern of behavior of Ferrar Glacier based on the assumption that ice can be modeled as a slowly flowing non-Newtonian fluid. This approximation, however, does not account for membrane-type ice flow, in which differential longitudinal strain reduces local driving stress variability and effectively ‘smooths out’ large along-flow velocity fluctuations. We account for the non-local modification of gravitational driving stresses by longitudinal stresses following the approach of *Kamb and Echelmeyer* [1986] and *Echelmeyer and Kamb* [1986]. Specifically, we apply an exponentially weighted averaging filter to calculated driving stress values, modified from theoretical maxima according to tabulated width-dependent shape factors ( $F$ ) that allow a portion of the gravitational force to be accommodated by valley sidewalls [*Cuffey and Paterson*, 2010], such that basal shear stress  $\tau_b$  is obtained from,

$$\tau_b = \frac{1}{2\ell H^{1/n}} \int \tau_d F H^{1/n} e^{-|\Delta x|/\ell} dx \quad (6)$$

where  $\ell$  represents longitudinal coupling length, the product of longitudinal coupling coefficient and ice thickness ( $H$ ). The integral spans a distance defined by the longitudinal averaging length, equal to  $4\ell$  [*Kamb and Echelmeyer*, 1986]. Driving stress ( $\tau_d$ ) arises from the usual relation:

$$\tau_d = -\frac{\partial S}{\partial x} \rho g H \quad (7)$$

in which  $-\partial S/\partial x$  defines the down-glacier surface slope.

[13] Based on the assumption of constant ice density throughout the glacier, we use Glen’s flow law to relate strain rate proportionally to the third power of the basal shear stress and calculate the deformation component of glacier velocity. Centerline surface velocities ( $u$ ) are then computed through addition of a basal sliding term:

$$u = f_d H \tau_b^n + f_s \frac{\tau_b^p}{H} \quad (8)$$

The temperature-dependent deformation rate parameter,  $f_d$ , above 263.15 K, depends on [*Cuffey and Paterson*, 2010]:

$$f_d = 240(n+1)^{-1} \quad (9)$$

where

$$A_0 = E \xi \exp \left( \frac{-Q}{R T} \right) \quad (10)$$

incorporating the activation energy necessary for creep ( $Q = 139 \text{ kJ mol}^{-1}$ ), the universal gas constant  $R$  ( $8.314 \text{ J mol}^{-1} \text{ K}^{-1}$ ), and a thermal parameter  $\xi$  ( $= 5.47 \times 10^{10}$ ) [*Hubbard*, 2006]. Below 263.15 K the value for creep activation energy is reduced to  $60 \text{ kJ mol}^{-1}$  [*Cuffey and Paterson*, 2010] and  $\xi = 1.14 \times 10^{-5}$ . In both cases we employ an enhancement coefficient ( $E$ ), as is typical of many Antarctic ice sheet models [e.g., *Takeda et al.*, 2002; *Parizek and Alley*, 2004; *Winkelmann et al.*, 2010], in order to account for softening of the ice (higher strain rate per unit stress) by impurities or contrasts in crystal orientation.

**Table 3.** Model Variables

Parameter	Symbol	Units
Driving stress	$\tau_d$	kPa
Basal shear stress	$\tau_b$	kPa
Ice surface elevation	$S$	m
Glacier width at bed	$w_b$	m
Cross-sectional area	$\gamma$	$m^2$
Shape factor	$F$	-
Distance along flowline	$x$	m
Ice thickness	$H$	m
Surface velocity	$u$	$m \text{ a}^{-1}$
Vertical velocity	$w$	$m \text{ a}^{-1}$
Vertical position in ice column	$z$	m
Sliding velocity component	$u_s$	$m \text{ a}^{-1}$
Deformation rate	$f_d$	$\text{kPa}^{-3} \text{ yr}^{-1}$
Arrhenius factor	$A_0$	$\text{kPa}^{-3} \text{ yr}^{-1}$
Longitudinal coupling length	$\ell$	m
Vertically integrated ice temperature	$\bar{T}$	K
Surface temperature	$T_s$	K
Basal ice temperature	$T_b$	K
Month of year	$m$	-
Annual air temperature range	$\Delta T_{ann}$	K
Net mass balance	$M$	$\text{m yr}^{-1}$
Effective precipitation rate at ice surface	$P_s$	$\text{m yr}^{-1}$
Sea level	$\psi$	m
Elevation of bed	$b$	m
Starting bed elevation	$b_0$	m
Till generation rate	$\varsigma$	-
Thickness of subglacial till layer	$H_\varphi$	m
Horizontal till flux	$Q_\varphi$	$\text{m}^2 \text{ yr}^{-1}$
Vertical distance from top of till layer	$z_\varphi$	m
Time	$t$	yr

[14] Sliding is governed by an exponential function [Hindmarsh and Le Meur, 2001] which allows sliding to occur over a range of temperatures close to the pressure-melting point, reflecting observations of basal ice motion at sub-freezing temperatures [Echelmeyer and Zhongxiang, 1987; Cuffey et al., 1999]:

$$f_s = f_{s0} \times \exp[-1 \times ((8.7 \times 10^{-4}H) - T_b)] \quad (11)$$

This scheme avoids numerical instabilities and the glaciological implausibility of having sliding take place only once the pressure-melting temperature has been reached.

#### 4.2. Mass Balance and Glacier Thermal Regime

[15] We prescribe climate boundary conditions, in the form of mean annual air temperature and precipitation at sea level and at altitude, on the basis of point observations and gridded data sets derived from regional observational data [Comiso, 1994; Morse et al., 1998; Vaughan et al., 1999; Monnin et al., 2004; Bliss et al., 2011]. Our parameterization of climate forcing does not take into account temporal or spatial variability (beyond the elevation dependence prescribed) known to result from changing oceanic and synoptic conditions [e.g., Morse et al., 1998; Bertler et al., 2004, 2006]. From these initial conditions we define perturbations representative of former cold (LGM) and warm (mid-Pliocene) conditions on the basis of ice core records [Morse et al., 1999; Monnin et al., 2004] and inferred from geological reconstructions [Staiger et al., 2006] (Table 1). For each climatic scenario, monthly mean ice surface temperatures ( $T_s^m$ ) are prescribed according to a simple

cosine function that defines a deviation from an annual mean ( $\bar{T}_s$ ).

$$T_s^m = \bar{T}_s - \left( \frac{\Delta T_{ann}}{2} \cos \left[ \frac{2\pi}{12} m \right] \right) \quad (12)$$

[16] Dry Valleys glaciers currently experience ablation almost solely as a consequence of sublimation, therefore we define net mass balance,  $M$  ( $\text{m a}^{-1}$ ), in the 300–1500 m elevation range according to an empirically derived relationship from neighboring Taylor Glacier [Bliss et al., 2011]:

$$M = \frac{0.35}{1500} \times S - 0.35 \quad (13)$$

A positive degree-day scheme is used to calculate surface melting if  $T_s^m \geq 0$ ,

$$M = \sum_{m=1}^{12} P_s^m - (T_s^m \times F_{pdd}) \quad (14)$$

where  $F_{pdd}$  is the melt coefficient, and  $P_s^m$  and  $T_s^m$  are effective monthly precipitation rate and monthly temperature at the glacier surface, respectively.

[17] Annual precipitation is distributed evenly throughout the year and assumed to equal surface accumulation where  $T_s^m \leq 0$ . Above this temperature, it is assumed that precipitation is liquid and is immediately lost from the system, thus effective precipitation,  $P = 0$ .

[18] Although we do not explicitly model the short floating portion of the Ferrar Glacier, we impose mass balance perturbations at the terminal end of the flowline such that ice grounded below sea level is affected by marine (in addition to atmospheric) ablation in one of two ways, depending on whether the ice thickness is above or below the flotation threshold  $H \leq (\psi - [b + H_\varphi]) \frac{\rho_w}{\rho}$ . In this manner we allow for the negative mass balance effects of sub-shelf melting, following Holland et al. [2008]:

$$M_{sh} = M - 0.341 T_o^2 + 2.365 T_o + 3.003 \quad (15)$$

and grounded margin (tidewater) calving [Cuffey and Paterson, 2010]

$$M_{tw} = M - \eta(c[\psi - b]) \quad (16)$$

in which  $\eta$  represents a scalable coefficient used as a tuning parameter, and  $c$  is a constant (Table 2). Geological data provide important guidance for our modeling experiments by quantifying, for example, the amount of terminus thickening likely to have occurred during the LGM ( $\approx 400$  m), relative to present [Denton and Marchant, 2000], or by identifying grounding zone retreat [Barrett et al., 1992; Barrett and Hambrey, 1992; Winter and Harwood, 1997] and increased sea surface temperatures [Winter et al., 2010, 2011], which we infer produced a land-terminating margin of the Ferrar Glacier during certain periods of the mid Pliocene.

[19] Temperatures at the glacier bed depend on ice surface temperatures (assumed here to equal air temperatures lapsed to elevation from a prescribed sea level value), geothermal heat flux ( $G$ ) and the thermal conductivity of ice ( $\kappa_{ice}$ ). Upward geothermal flux ( $68 \text{ mW m}^{-2}$  [Shapiro and

*Ritzwoller*, 2004]) is opposed by the downward advection of colder ice at a rate ( $w$ ) governed by the net mass balance. Strain heating (dissipation), heat of sliding friction, and a horizontal advection term further modify basal temperatures [Hindmarsh, 1999; Cuffey and Paterson, 2010], which are then adjusted for pressure melting to yield ‘effective’ temperature [Hindmarsh and Le Meur, 2001]:

$$\begin{aligned} T_b = T_s + \left( \frac{G H}{\kappa_{ice}} \right) + (8.7 \times 10^{-4} H) - \left( u \frac{\partial T}{\partial x} + w \frac{\partial T}{\partial z} \right) \\ + \left( 2 \frac{\partial \bar{u}}{\partial x} \times \tau_b \right) + (\tau_b u_s) \end{aligned} \quad (17)$$

[20] Horizontal and vertical temperature gradients at each timestep are computed from the previous temperature solution; basal temperatures are capped at the pressure melting point, such that excess heat energy is essentially lost from the system. Acknowledging the limitations of our vertically averaged ice flow model and the concomitant difficulties in constraining the shape of the glacier temperature-depth profile, we follow *Kavanaugh and Cuffey* [2009] and assume a linear vertical temperature gradient throughout the glacier and from this calculate a mean ice temperature for the subsequent computation of the ice deformation rate (equation (10)). Due to the exponential decrease in ice hardness with increasing temperatures, errors in the temperature solution may significantly influence glacier velocities. However, by using a flow rate enhancement factor ( $E$ ) to tune modeled velocities to observed values, the impact of such errors may be reduced.

#### 4.3. Bedrock Erosion and Till Flux

[21] Subglacial erosion of bedrock may occur due to plucking, abrasion, or fracturing in response to unloading. The relative dominance of each process in time and space depends largely on temperature and pressure conditions at the bed, abundance and physical characteristics of subglacial debris already entrained in the basal ice, and ice dynamics. In terms of our relatively coarse horizontal model resolution, most, if not all, of these factors are essentially sub-grid scale. We therefore follow *Pollard and DeConto* [2003] and simply consider the integrated effect of these processes by calculating bedrock erosion from basal shear stress and sliding velocity, scaled according to a prescribed erosion coefficient and controlled by a modifier such that the till generation rate ( $\varsigma$ ) decreases as till thickness approaches a prescribed maximum value:

$$\varsigma = 0.2 \times 10^{-9} \tau_b u_s \left( 1 - \frac{H_\varphi}{\varphi_{max}} \right) \quad (18)$$

[22] This scheme, however, neglects spatial variability in the propensity of bedrock to erode, which may be caused by contrasts in its strength (related to lithology and loading history), and surface roughness (which affects plucking). While recognizing these limitations, we justify our approach on the basis that our investigation is principally aimed at exploring differences between modeled scenarios, rather than at accurately quantifying sediment volumes. Sediment production is regulated by prescribing an erosion-limiting till thickness ( $\varphi_{max}$ ). The inclusion of this parameter is justified by studies that have identified reductions in bed-

rock quarrying as deforming layer thicknesses increase [Iverson, 1991; Cuffey and Alley, 1996; Alley, 2000], thereby imposing a limiting feedback. In our model, we propose that the limiting thickness of till is equal to the maximum thickness to which subglacial shearing occurs, such that beyond the depth to which horizontal ice velocities are propagated, bedrock erosion tends toward zero. Erosion at intermediate till thicknesses is governed by an exponential relationship that defines substrate velocity.

[23] In order to calculate flux of subglacial substrate in the till column at each node of our staggered grid, we employ a physically based, but heuristic, method. Following a similar approach to that of *Alley* [1989] and *Fowler* [2000], our scheme exponentially relates basal sliding velocity of the glacier to horizontal velocity (and hence flux) of the substrate. Flux of the till layer at each grid point ( $Q_\varphi$ ) is therefore given by:

$$Q_\varphi = \int_0^{\varphi_{max}} u_s^{(1-(z_\varphi/\varphi_{max}))} dz_\varphi \quad (19)$$

with substrate layer evolution through time described by:

$$\frac{\partial H_\varphi}{\partial t} = \frac{\partial Q_\varphi}{\partial x} + \varsigma \quad (20)$$

[24] We make an assumption of perfect ice-till coupling, but recognize that this scenario represents an ‘end-member of a spectrum of possible behaviors’ [Alley *et al.*, 1987, p. 8924]. Modifying the degree of coupling would influence the magnitude, but not the distribution, of our modeled till thicknesses. As noted by *Fowler* [2000], integrated till flux is an increasing function of velocity through a mutual dependence on shear stress at the glacier bed. In contrast to *Fowler* [2000], however, our method imposes a limiting substrate thickness beyond which flux is negligible. Prescription of this condition is motivated by research indicating that deforming layer thicknesses are usually finite [*Piotrowski et al.*, 2004; *Kjær et al.*, 2007], and commonly  $\leq 2$  m (*Piotrowski et al.* [2006] report a deforming layer thickness of only c. 0.5 m). In terms of our predictions of subglacial processes, we acknowledge the considerable uncertainty that surrounds the mechanisms and rates by which glaciers erode and transport subglacial material, and defend our calculation, based on a vertical integration of an empirically guided exponential-based till velocity field, on the grounds that its complexity is sufficient for the elucidation of first-order differences between contrasting environmental forcings during the LGM, Present and mid-Pliocene.

#### 4.4. Isostatic Loading and Evolution of Bed Elevation

[25] Elevation of the glacier bed evolves according to pointwise isostatic depression imposed through ice loading [*van der Veen*, 1999], and the rate of bedrock erosion. We start from an assumption of local isostatic equilibrium, and calculate transient changes in bedrock elevation according to changes in ice thickness from present, modulated by a mantle relaxation timescale ( $\theta$ ) of 3 kyr [*Huybrechts*, 1993; *Pattyn*, 2006; *De Boer et al.*, 2010] (equation (21)).

$$\frac{\partial b}{\partial t} = \left( \frac{1}{\theta} \left[ b_0 - b - \frac{\rho}{\rho_m} H \right] \right) - \varsigma \quad (21)$$

Although this approach may be better suited to changes over longer wavelengths than that of our domain, we consider it nonetheless applicable here for the following reasons. Firstly, our simulations are of steady state conditions, under which crustal loading has also reached equilibrium. Secondly, although we model Ferrar Glacier in isolation, we envisage that the simulated changes in ice thickness reflect a regional scale ice sheet response to climatic perturbations. Thus, while regional effects arising from changes in ice loading beyond the domain are not explicitly accounted for, our local isostatic scheme implicitly assumes that crustal depression within the domain is likely the result of ice mass changes in the wider area. Third, our simulated changes in ice thickness are relatively small (10's – 100's m) thus although we cannot completely discount the possibility that subtleties of the simulated time-dependent response of the bed to changes in loading may influence modeled ice geometry, we consider such effects to be relatively minor. A final point is that the style of likely crustal response to loading in this domain, straddling the uplifted rift shoulder of the Transantarctic Mountains and the adjacent subsiding Victoria Land Basin, may be one of both flexure and elastic failure [Bott and Stern, 1992], thus difficult to parameterize in a simple model such as ours. Ice surface height at the end of each time step is then given by:

$$S = b + H_\varphi + H \quad (22)$$

## 5. Results

### 5.1. Diagnostic Simulation

[26] The first aim of our investigation was to carry out an isochronous simulation of Ferrar Glacier under present conditions, in order to acquire new insight into the possible glaciological conditions that give rise to the observed dynamical behavior. The velocity field that results from the bed iteration procedure is similar both in magnitude and pattern to the one derived from InSAR data (Figure 4), and has generally smaller mismatches than those produced from the initializing (Calkin) data set (Figure 5). However, despite extensive exploration of sliding and deformation rate parameterizations, the agreement between modeled and observed velocities remains imperfect, no doubt reflecting simplifications in the physics of our model. These reservations notwithstanding, the model's ability to simulate Ferrar Glacier dynamics that are sufficiently representative of its present-day character gives us confidence in our adoption of this parameter set for subsequent experimentation. Our diagnostic model of Ferrar Glacier uses the iterated ice thickness values, holds constant the surface profile recorded by Calkin [1974] and calculates internal variables (temperature, rheology, balance of sliding/deformation) based on the tuning of flow parameters undertaken during the bed iteration stage. In order to adequately take account of non-local effects, we apply an exponentially weighted variable-length averaging filter [Kamb and Echelmeyer, 1986] to our predicted driving stresses, and calculate glacier velocities from the smoothed basal shear stress values (Figure 6). Experimentation revealed that the most acceptable results could be obtained with the coupling coefficient = 5, and the longitudinal averaging length = 4  $\ell$ . The resulting pattern of longitudinally averaged shear stress variability closely

follows that of the driving stress, but exhibits considerably lower curvature, with lowered peaks and less deep troughs. That the longitudinal coupling length is dependent on ice thickness is illustrated in the much smoother stress distribution in the upper Ferrar (where the glacier is thickest), compared to the more variable stress regime nearer the terminus where the ice is thinnest. Thus whereas highest driving stresses are largely related to steep surface gradients, their ability to influence flow of the glacier as a whole is modulated by the depth of ice that experiences the slope. Consequently, steep gradients in relatively thin areas of the lower Ferrar result in only local accelerations, whereas flow velocities in the thicker upper Ferrar tend to reflect the surface profile over a much greater length-scale (Figure 4).

[27] Given these results, it is perhaps not surprising that the model is best able to simulate observed velocities in areas where flow is controlled by more general glacier geometry, and conversely struggles most in areas of thin ice where dynamics are locally controlled and therefore most susceptible to limitations of the model or input data. In general, however, modeled velocities are close both in distribution and magnitude to those interpreted from InSAR [Kavanaugh et al., 2009a] in all but a few areas, especially when the diagnostic simulation uses the iterative scheme to modify the bed profile (Figure 5). Comparing modeled velocities against geometric variables (Figure 2) it is apparent that zones of accelerating flow are associated with a combination of steepening surface slope and thinning of the glacier, although neither one of these factors is solely responsible for the observed flow pattern. Thus Ferrar Glacier currently appears to flow most vigorously where it flows over and away from large undulations in its bed, regardless of whether these bumps are close to the surface or not. Flow is most sluggish where changes in the cross-sectional valley geometry allow a greater volume of ice to be accommodated than immediately upstream, for example where the valley rapidly widens or where the valley floor deepens.

### 5.2. Time-Dependent Simulations

#### 5.2.1. Last Glacial Maximum

[28] The second aim of our study was to use the model to investigate possible variations in glacial dynamics under colder and drier conditions (LGM), and warmer and wetter environments (mid-Pliocene). In contrast to the diagnostic run described above, in these experiments we allow the surface to evolve freely for 10000 model years, by which time a steady state glacier configuration has more-or-less been reached. Figure 7a illustrates the modeled ice surface under these conditions. Geological evidence suggests that the LGM glacier profile was considerably shallower than at present, with thicker ice where the glacier was confluent with the expanded LGM ice sheet grounded in the present-day Ross Sea. Simulating this geometry, our calculation of basal temperatures shows that the LGM glacier hosted only small areas close to (or at) the pressure melting point beneath the thickest ice. Since glacier velocities are intrinsically linked with climate (through accumulation rate and temperature), our LGM model predicts very low deformation velocities (typically  $<10 \text{ ma}^{-1}$ ), and only very restricted sliding where basal temperatures are close to the pressure melting point. As a consequence of near-zero basal sliding along most of the glacier, bedrock erosion rate and the

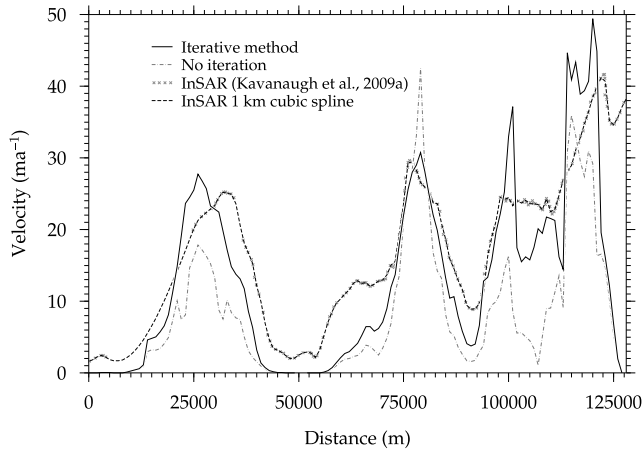


**Figure 4.** Diagnostic surface velocity field compared to ‘observed’ values derived from InSAR [Kavanaugh *et al.*, 2009a]. Note the improvement achieved using the iterated bed method. Figure also shows cubic spline used to fill data gaps in the InSAR data.

generation of basal till are minimal. The greater ice load imposed by the thickened lower Ferrar results in additional depression of the bed compared to present, whereas thinning in mid-sections of the glacier allows a small amount of isostatic rebound to occur. After 10000 model years, the LGM glacier exhibits a steady state volume c. 16.0% lower than at the start of the run.

### 5.2.2. Present

[29] Under present conditions, our model predicts areas of wet-based ice only in the deeper basins, both in the upper and lower Ferrar (Figure 7b). This representation of a

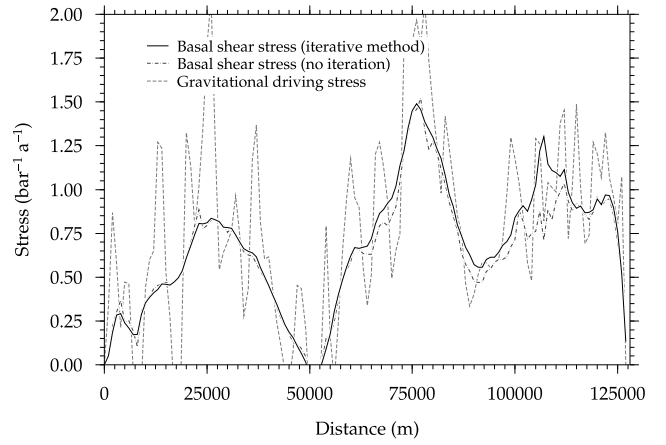


**Figure 6.** Gravitational driving stresses and basal shear stresses along the glacier flowline, illustrating the variable degree of smoothing arising from the latter’s dependence on ice thickness.

largely cold-based Ferrar glacier is more similar to the findings of Kavanaugh and Cuffey [2009] on neighboring Taylor Glacier, who noted that basal temperatures were close to pressure melting only under kilometer-thick ice, than to the calculations of Robinson [1984], also on Taylor Glacier, who proposed that as much as half of the lower ablation area may be melting at its base. While our predicted velocity fields show only very restricted areas of basal sliding, warmer temperatures throughout the ice column coupled with a greater accumulation rate lead to significantly higher deformation velocities than those under the LGM regime. Modeled bedrock erosion rates and basal till flux are low throughout the domain, as a consequence of only very limited basal sliding (Figure 7d). Nonetheless, the predicted foci of till accumulation compare well with geological evidence from formerly glaciated terrains which report preferential deposition of till in basins and against reverse slopes [Thorp, 1991]. In our model, deposition occurs across the width of basins in the lower Ferrar, but is thickest at the transition from sliding to non-sliding ice where a positive till flux imbalance occurs. By the end of the simulation, modeled ice volume in the domain is 99.6% of its initial value, with a rate of change of  $<0.001\text{ a}^{-1}$ .

### 5.2.3. Episodes of Peak Warmth, Mid-Pliocene

[30] Geological studies have indicated that during warm episodes in the mid-Pliocene, ocean-atmosphere conditions produced a glacier profile similar in its upper reaches to that of present, but considerably shorter in length and therefore steeper in overall gradient. In reproducing this geometry (Figure 7a), our model predicts a basal thermal regime that is characterized by a majority of the bed at or near the pressure melting temperature, with cold-based zones only where the ice surface elevation is high or the glacier is thin (Figure 7b). The combination of relatively high atmospheric temperature and precipitation with ice largely at the pressure melting point produces a glacier that is relatively fast-flowing ( $>20\text{ ma}^{-1}$ ) throughout the valley-confined sector, and slow only in the upper plateau area (Figure 7c). Surface velocities exceed  $50\text{ ma}^{-1}$  up-glacier of the terminus, where both ice surface and bed gradients are particularly steep. Basal sliding is more extensive than under other

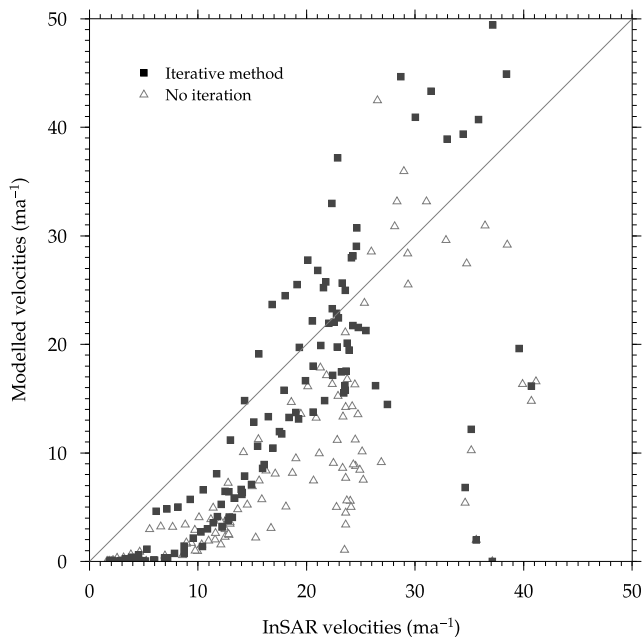


**Figure 5.** Modeled versus observed glacier velocities, showing reduced overall mismatch using the iterated ice thickness/bed profile compared with those derived from the unadjusted Calkin [1974] radar profile.

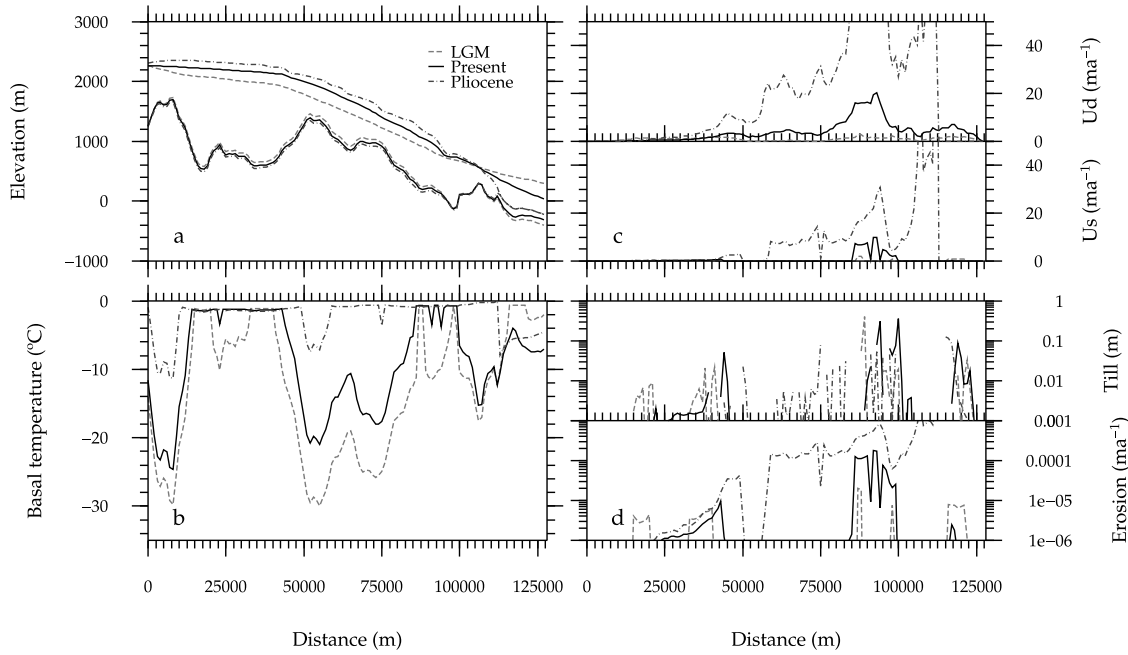


**Figure 7.** Simulated Ferrar Glacier configurations under cold (Last Glacial Maximum), interglacial (Present), and warm (mid-Pliocene) conditions. Note (a) lower surface slope, (b) lower basal temperatures, (c) slower velocities and (d) lower erosion rates of the modeled glacier under colder conditions, with a more dynamic and erosive glacier (faster, warmer, steeper) under warmer climates.

climates, but creep still dominates in the contribution that it makes to total glacier motion. Nonetheless, the higher sliding velocities in the modeled mid-Pliocene Ferrar Glacier give rise to a much more active basal substrate, with till thickness 1–2 orders of magnitude greater than those simulated under LGM and Present scenarios (Figure 7d). Changes in the long-profile of the Pliocene glacier compared to present may, if sufficiently long-lived, have resulted in marked isostatic adjustments of the bed during this time, most likely characterized by crustal rebound in the deglaciated part of the domain and enhanced depression of the bed beneath the thickened upper sector. Modeled volume at the end of the run is 7.7% greater than at initialization, and is still increasing, albeit slowly, at a rate of  $0.001\text{ a}^{-1}$ .

## 6. Discussion

[31] In earlier papers, *Kavanaugh et al.* [2009a, 2009b] and *Kavanaugh and Cuffey* [2009] questioned the reliability of the *Calkin* [1974] radar profiles of Taylor and Ferrar glaciers. Yet these data remain the most detailed source of ice thickness interpretations along Ferrar Glacier and are therefore intrinsically valuable. Here we have sought to improve the usability of the radar bed profile by adopting an inverse approach that takes observed centerline velocities as input. The forward model uses an initial parameterization of sliding and deformation rates and iteratively adjusts bed elevations where necessary in order that modeled velocities are as close as possible to the input data without introducing implausibly abrupt thickness changes. This approach has enabled a more accurate simulation of Ferrar Glacier dynamics, and thus we suggest that our predicted bed profile may be closer to reality than that revealed in the *Calkin* radar data.

[32] Using this calculation of bed depth and ice thickness, our model of Ferrar Glacier shows that fastest flow occurs as a consequence of surface geometry and changes in valley cross-profile. Longitudinal flow variability arises from mass conservation, in which flux imbalance is avoided by dynamic adjustment to changing geometry. The glacier thickens upstream of large bed undulations and subsequently accelerates over their crests due to steepened downglacier surface gradients. Changes in valley width may also exert a second-order control. The along-flow influence of these accelerating zones is modulated by glacier thickness, such that the effects are most extensively propagated in areas of thick ice, but are only locally significant in areas where the glacier is thin. These results allow a new perspective on recent debate surrounding the likely flow mechanisms of Transantarctic Mountain glaciers. In a study of Ferrar Glacier, *Johnson and Staiger* [2007] proposed that two topographic ‘dams’ exist beneath the glacier, which influence its flow regime to such a great extent that they almost completely impede ice flux, giving rise to very low surface velocities throughout the glacier and minima located above the bedrock ridges. This interpretation was subsequently criticized by *Kavanaugh and Cuffey* [2009] and *Kavanaugh et al.* [2009a, 2009b], however, both on theoretical grounds and on the basis of their detailed empirical and numerical analysis of neighboring Taylor Glacier. These authors suggested instead that EAIS outlet glaciers such as Taylor and Ferrar ‘cascade’ over bedrock obstacles by thinning and accelerating over obstructions, and slowing across deeper basins. Our results, therefore, find greater agreement with the model of glacier flow proposed by *Kavanaugh et al.* [2009a] than with that of *Johnson and Staiger* [2007].

[33] A second focus of this study has been the competing hypotheses that argue either for long-term stability [Denton *et al.*, 1993; Sugden *et al.*, 1993; Staiger *et al.*, 2006], or dynamic oscillations [Webb *et al.*, 1984; Barrett *et al.*, 1992; Wilson, 1995; McKelvey *et al.*, 2004; Prentice and Krusic, 2005; Naish *et al.*, 2009], of the East Antarctic Ice Sheet over the last 5 Myr. In essence, the former propose that much of the Victoria Land landscape is a relic of Miocene times, with the key fjords (such as Ferrar) incised before the Pliocene. The main glaciological change envisaged in this area during Pliocene warming was a modest thickening of outlet glaciers [Marchant *et al.*, 1994; Hall *et al.*, 1997] in response to increased accumulation, in a manner akin to that inferred for the early Holocene [Domack *et al.*, 1991; Steig *et al.*, 2000]. In contrast, others have suggested that large-scale deglaciation of East Antarctica took place during the Pliocene [Webb and Harwood, 1991], promoted by warmer coastal ocean water [Abelmann *et al.*, 1990; Ishman and Rieck, 1992] that led to a pre-Pleistocene ice sheet characterized by a ‘lower profile’ than today [Webb and Harwood, 1991, p. 220]. In attempting to find some common ground between these theories, Hall *et al.* [1997] and Siegert *et al.* [2008] suggest that the EAIS maintained a cold, stable core during the warm parts of the Pliocene, but fed warm, marine-based, dynamic outlet glaciers around its margins.

[34] The modeling results presented above indicate that the Ferrar Glacier responds to perturbed environmental forcing in a relatively simple manner. Under colder, drier, regimes a lower gradient outlet glacier develops that is starved in its upper catchment and experiences only limited mass loss at its terminus/lowest confluence. Our model reproduces the thinning at higher elevations and expansion in the lower reaches of the glacier shown by geological evidence both along the Transantarctic Mountains [Bockheim *et al.*, 1989; Denton and Hughes, 2000; Bromley *et al.*, 2010] and EAIS margins further afield [Lilly *et al.*, 2010; Mackintosh *et al.*, 2011], constituting an overall reduction in total ice volume within our domain (although this does not encompass the entire extent of the expanded LGM outlet glacier). As a consequence of its low longitudinal profile, cold atmospheric temperatures and decreased surface accumulation, the simulated LGM glacier is sluggish and moves almost exclusively by deforming internally, with little to no erosion of its bed. A higher or lower confluence with grounded ice of the LGM ice sheet in the Ross Sea would, respectively, reduce or increase Ferrar Glacier velocities due to the change in overall surface gradient, thus modest acceleration during deglaciation would seem likely. At the coldest stage of this and most probably other glacial cycles, however, the geological imprint left by subglacial processes in this environment was likely subtle. Moraine formation may have been controlled instead by subaerial processes at glacier margins. Under warmer than present (e.g., mid-Pliocene) conditions, the prescribed wetter environment leads to a modeled ice thickness that is slightly greater than that of present in the upper reaches of Ferrar Glacier, but which is thinner and less extensive close to modern sea level. A net increase in modeled ice volume with respect to both present and LGM simulations reflects the higher accumulation rates under warmer Pliocene conditions. The simulated Pliocene glacier is relatively dynamic, with abundant basal sliding, erosion of bedrock, and transport of till toward the terminus.

Basal and surface melt would likely give rise to sub- and proglacial drainage systems carrying suspended debris into the proximal Ross Sea. Glaciomarine facies identified in the CIROS-2 sediment core (Figure 1) may reflect such an origin [Barrett and Hambrey, 1992].

[35] We suggest that these results go some way toward reconciling the divergent views concerning the long-term (in)stability of EAIS outlet glaciers, by offering an alternative scenario in which, under warmer climates, these distributaries experience considerable geometric (thickness, length) changes near their margins, and undergo a significant evolution of their dynamics throughout the majority of their length. Ongoing volumetric change (albeit small) at the end of our warm-climate simulation implies a glacier response time during retreat in the order of  $1 \times 10^4$  years, with perhaps a slightly lower value during cold-climate advances. The cause and significance of this possibly non-linear volumetric response of Transantarctic Mountain glaciers to climate change remains a future research focus.

## 7. Conclusions

[36] The dynamic behavior of outlet glaciers draining the East Antarctic Ice Sheet toward the Ross Sea embayment both at present and during the recent geological past has been the source of considerable uncertainty for several decades, with the consequence that widely divergent glaciological and paleoenvironmental scenarios have been proposed. We have attempted to numerically simulate one such outlet, Ferrar Glacier, under present-day environmental conditions, and to validate our results against empirical data pertinent to both geometry (airborne radar profiles) and dynamics (InSAR velocities). Subsequently we have used this validated model to predict possible responses of the glacier to colder (LGM) and warmer (mid-Pliocene) climates, using geological and ice core data for constraint. We argue that the glacier is largely cold-based under present conditions, and flows predominantly by way of internal deformation with only local areas of basal sliding. We find no evidence to support previous suggestions that topographic ‘dams’ beneath the glacier retard flow [Johnson and Staiger, 2007]. Rather, we concur with Kavanagh *et al.* [2009a] that the Ferrar Glacier flows fastest where it ‘cascades’ over these bedrock bumps. Climates that were colder and drier than present, such as those that characterized the Last Glacial Maximum, led to a lower mean surface gradient that produced a more slowly flowing glacier, whereas warmer climates, such as during the mid-Pliocene, brought about a more active glacier that was most likely warm-based and sliding across much of its bed. These model results therefore find agreement both with theories of long-term stability in the upper reaches of outlet glaciers [Sugden *et al.*, 1993], and with proposals of more dynamic glaciers in lower, valley-confined, areas and ice-mass loss at the continental margin [Barrett and Hambrey, 1992; Ishman and Rieck, 1992; Naish *et al.*, 2009].

[37] **Acknowledgments.** This work was supported by the Alan Eggers postdoctoral fellowship to N.G. and by FRST funding to R.L. The authors are particularly grateful to Brian Anderson, Frank Kane, Andrew Mackintosh, and Peter Barrett for useful discussions; to Kurt Cuffey and Andy Bliss for providing unpublished ablation data from Taylor Glacier;

and to Dick Peltier and Rosemarie Drummond for LGM relative sea level data. We are also especially grateful to Duncan Young and Don Blankenship for providing unpublished radar data for a section of the lower Ferrar, arising from NSF grant ANT-0733025 to the University of Texas, NASA grant NNX09AR52G and NERC grant NE/D00373/1. Insightful and detailed comments from Kurt Cuffey and Associate Editor Martin Truffer, as well as those of the anonymous reviewers, significantly improved this paper.

## References

- Abelmann, A., R. Gersonde, and V. Spiess (1990), Pliocene-Pleistocene paleoceanography in the Weddell Sea: Silicic microfossil evidence, in *Geological History of the Polar Oceans: Arctic Versus Antarctic*, edited by U. Bleil and J. Theide, pp. 729–759, Kluwer, Dordrecht, Netherlands.
- Alley, R. B. (1989), Water-pressure coupling of sliding and bed deformation: II. Velocity-depth profiles, *J. Glaciol.*, 35(119), 119–129.
- Alley, R. B. (2000), Continuity comes first: Recent progress in understanding subglacial deformation, in *Deformation of Glacial Materials*, edited by A. J. Maltman, B. Hubbard, and M. J. Hambrey, *Geol. Soc. Spec. Publ.*, 176, 171–179.
- Alley, R. B., D. D. Blankenship, C. R. Bentley, and S. T. Rooney (1987), Till beneath ice stream B, 3. Till deformation: Evidence and implications, *J. Geophys. Res.*, 92(B9), 8921–8929.
- Bamber, J. L., J. L. Gomez-Dans, and J. A. Griggs (2009), A new 1 km digital elevation model of the Antarctic derived from combined satellite radar and laser data—Part 1: Data and methods, *Cryosphere*, 3, 101–111.
- Barrett, P. J., and M. J. Hambrey (1992), Plio-Pleistocene sedimentation in Ferrar Fjord, Antarctica, *Sedimentology*, 39(1), 109–123.
- Barrett, P. J., C. J. Adams, W. C. McIntosh, C. C. Swisher, and G. S. Wilson (1992), Geochronological evidence supporting Antarctic deglaciation 3 million years ago, *Nature*, 359(6398), 816–818.
- Bertler, N. A. N., P. J. Barrett, P. A. Mayewski, R. L. Fogt, K. J. Kreutz, and J. Shulmeister (2004), El Niño suppresses Antarctic warming, *Geophys. Res. Lett.*, 31, L15207, doi:10.1029/2004GL020749.
- Bertler, N. A. N., T. R. Naish, H. Oerter, S. Kipfstuhl, P. J. Barrett, P. A. Mayewski, and K. Kreutz (2006), The effects of joint ENSO–Antarctic Oscillation forcing on the McMurdo Dry Valleys, Antarctica, *Antarct. Sci.*, 18, 507–514.
- Bliss, A. K., K. M. Cuffey, and J. Kavanaugh (2011), Sublimation and surface energy budget of Taylor Glacier, Antarctica, *J. Glaciol.*, 57(204), 684–696.
- Bockheim, J. G., S. C. Wilson, G. H. Denton, B. G. Andersen, and M. Stuiver (1989), Late Quaternary ice-surface fluctuations of Hatherton Glacier, Transantarctic Mountains, *Quat. Res.*, 31(2), 229–254.
- Bott, M., and T. Stern (1992), Finite element analysis of Transantarctic Mountain uplift and coeval subsidence in the Ross Embayment, *Tectonophysics*, 20(3–4), 341–356.
- Bromley, G., B. Hall, J. Stone, H. Conway, and C. Todd (2010), Late Cenozoic deposits at Reedy Glacier, Transantarctic Mountains: implications for former thickness of the West Antarctic Ice Sheet, *Quat. Sci. Rev.*, 29(3–4), 384–398.
- Calkin, P. E. (1974), Subglacial geomorphology surrounding the ice-free valleys of Southern Victoria Land, Antarctica, *J. Glaciol.*, 13, 415–429.
- Chen, J. L., C. R. Wilson, D. Blankenship, and B. D. Tapley (2009), Accelerated Antarctic ice loss from satellite gravity measurements, *Nat. Geosci.*, 2, 859–862.
- Comiso, J. C. (1994), Surface temperatures in the polar regions from Nimbus 7 temperature humidity infrared radiometer, *J. Geophys. Res.*, 99(C3), 5181–5200.
- Conway, H., B. L. Hall, G. H. Denton, A. M. Gades, and E. D. Waddington (1999), Past and future grounding-line retreat of the West Antarctic Ice Sheet, *Science*, 286(5438), 280–283.
- Cuffey, K., and R. B. Alley (1996), Is erosion by deforming subglacial sediments significant? (Toward till continuity), *Ann. Glaciol.*, 22, 17–24.
- Cuffey, K., and W. S. B. Paterson (2010), *The Physics of Glaciers*, Butterworth-Heinemann, Oxford, U. K.
- Cuffey, K. M., H. Conway, B. Hallet, A. M. Gades, and C. F. Raymond (1999), Interfacial water in polar glaciers and glacier sliding at  $-17^{\circ}\text{C}$ , *Geophys. Res. Lett.*, 26(6), 751–754.
- De Boer, B., R. S. W. Van De Wal, R. Bintanja, L. J. Lourens, and E. Tuenter (2010), Cenozoic global ice-volume and temperature simulations with 1-D ice-sheet models forced by benthic  $\delta^{18}\text{O}$  records, *Ann. Glaciol.*, 51, 23–33.
- Denton, G. H., and T. J. Hughes (2000), Reconstruction of the Ross ice drainage system, Antarctica, at the last glacial maximum, *Geogr. Ann. Ser. A*, 82, 143–166.
- Denton, G. H., and D. R. Marchant (2000), The geologic basis for a reconstruction of a grounded ice sheet in McMurdo Sound, Antarctica, at the Last Glacial Maximum, *Geogr. Ann. Ser. A*, 82, 167–211.
- Denton, G. H., J. G. Bockheim, S. C. Wilson, and M. Stuiver (1989), Late Wisconsin and early Holocene glacial history, inner Ross embayment, Antarctica, *Quat. Res.*, 31(2), 151–182.
- Denton, G. H., D. E. Sugden, D. R. Marchant, B. L. Hall, and T. I. Wilch (1993), East Antarctic Ice Sheet sensitivity to Pliocene climatic change from a Dry Valleys perspective, *Geogr. Ann. Ser. A*, 75, 155–204.
- Domack, E. W., A. J. T. Jull, and S. Nakao (1991), Advance of East Antarctic outlet glaciers during the hypsithermal: Implications for the volume state of the Antarctic ice sheet under global warming, *Geology*, 19, 1059–1062.
- Dwyer, G., and M. Chandler (2009), Mid-Pliocene sea level and continental ice volume based on coupled benthic Mg/Ca palaeotemperatures and oxygen isotopes, *Philos. Trans. R. Soc. A*, 367(1886), 157–168.
- Echelmeyer, K. A., and B. Kamb (1986), Stress-gradient coupling in glacier flow: II. Longitudinal averaging of the flow response to small perturbations in ice thickness and surface slope, *J. Glaciol.*, 32, 285–298.
- Echelmeyer, K., and W. Zhongxiang (1987), Direct observation of basal sliding and deformation of basal drift at sub-freezing temperatures, *J. Glaciol.*, 33, 83–98.
- Fowler, A. C. (2000), An instability mechanism for drumlin formation, in *Deformation of Glacial Materials*, edited by A. J. Maltman, B. Hubbard, and M. J. Hambrey, *Geol. Soc. Spec. Publ.*, 176, 307–319.
- Hall, B. L., G. H. Denton, D. R. Lux, and C. Schlüchter (1997), Pliocene palaeoenvironment and Antarctic ice sheet behaviour: Evidence from Wright Valley, *J. Geol.*, 105, 285–294.
- Hindmarsh, R. C. A. (1999), On the numerical computation of temperature in an ice sheet, *J. Glaciol.*, 45, 568–574.
- Hindmarsh, R. C. A. (2001), Notes on basic glaciological computational methods and algorithms, in *Continuum Mechanics and Applications In Geophysics and the Environment*, pp. 222–249, Springer, New York.
- Hindmarsh, R. C. A., and E. Le Meur (2001), Dynamical processes involved in the retreat of marine ice sheets, *J. Glaciol.*, 47, 271–282.
- Holland, P. R., A. Jenkins, and D. M. Holland (2008), The response of ice shelf basal melting to variations in ocean temperature, *J. Clim.*, 21(11), 2558–2572, doi:10.1175/2007JCLI1909.1.
- Hubbard, A. (2006), The validation and sensitivity of a model of the icelandic ice sheet, *Quat. Sci. Rev.*, 25, 2297–2313.
- Huybrechts, P. (1993), Glaciological modelling of the Late Cenozoic East Antarctic ice sheet: stability or dynamism?, *Geogr. Ann. Ser. A*, 75, 221–238.
- Ishman, S. E., and H. J. Rieck (1992), A late Neogene Antarctic glacio-eustatic record, Victoria Land Basin margin, Antarctica, in *The Antarctic Paleoenvironment: A Perspective on Global Change*, *Antarct. Res. Ser.*, vol. 56, edited by J. P. Kennett and D. A. Warnke, pp. 327–347, AGU, Washington, D. C.
- Iverson, N. R. (1991), Potential effects of subglacial water-pressure fluctuations on quarrying, *J. Glaciol.*, 37(125), 27–36.
- Johnson, J. V., and J. W. Staiger (2007), Modeling long-term stability of the Ferrar Glacier, East Antarctica: Implications for interpreting cosmogenic nuclide inheritance, *J. Geophys. Res.*, 112, F03S30, doi:10.1029/2006FJ000599.
- Joughin, I., D. MacAyeal, and S. Tulaczyk (2004), Basal shear stress of the Ross ice streams from control method inversions, *J. Geophys. Res.*, 109, B09405, doi:10.1029/2003JB002960.
- Kamb, B., and K. A. Echelmeyer (1986), Stress-gradient coupling in glacier flow: I. Longitudinal averaging of the influence of ice thickness and surface slope, *J. Glaciol.*, 32, 267–284.
- Kavanaugh, J. L., and K. M. Cuffey (2009), Dynamics and mass balance of Taylor Glacier, Antarctica: 2. Force balance and longitudinal coupling, *J. Geophys. Res.*, 114, F04011, doi:10.1029/2009FJ001329.
- Kavanaugh, J. L., K. Cuffey, D. L. Morse, H. Conway, and E. Rignot (2009a), Dynamics and mass balance of Taylor Glacier, Antarctica: 1. Geometry and surface velocities, *J. Geophys. Res.*, 114, F04010, doi:10.1029/2009FJ001309.
- Kavanaugh, J. L., K. Cuffey, D. L. Morse, A. K. Bliss, and S. M. Aciego (2009b), Dynamics and mass balance of Taylor Glacier, Antarctica: 3. State of mass balance, *J. Geophys. Res.*, 114, F04012, doi:10.1029/2009FJ001331.
- Kjær, K. H., E. Larsen, J. J. M. van der Meer, O. Ingólfsson, J. Krüger, I. O. Benediktsson, C. G. Knudsen, and A. Schomacker (2007), Subglacial decoupling at the sediment/bedrock interface: a new mechanism for rapid flowing ice, *Quat. Sci. Rev.*, 25, 2704–2712.
- Le Brocq, A., A. Payne, and A. Vieli (2010), An improved Antarctic dataset for high resolution numerical ice sheet models (ALBMAP v1), *Earth Syst. Sci. Data*, 2, 247–260, doi:10.5194/essd-2-247-2010.
- Lilly, K., D. Fink, D. Fabel, and K. Lambeck (2010), Pleistocene dynamics of the interior East Antarctic ice sheet, *Geology*, 38(8), 703–706.
- Liu, H., and K. C. Jezek (2004), A complete high-resolution coastline of Antarctica extracted from orthorectified radarsat SAR imagery, *Photogramm. Eng. Remote Sens.*, 70(5), 605–616.

- MacAyeal, D. (1993), A tutorial on the use of control methods in ice-sheet modeling, *J. Glaciol.*, 39(131), 91–98.
- Mackintosh, A., et al. (2011), Retreat of the East Antarctic ice sheet during the last glacial termination, *Nat. Geosci.*, 4(3), 195–202, doi:10.1038/ngeo1061.
- Marchant, D., G. Denton, and C. Swisher III (1993), Miocene-Pliocene-Pleistocene glacial history of Arena Valley, Quartermain Mountains, Antarctica, *Geograf. Ann.*, Ser. A, 75(4), 269–302.
- Marchant, D. R., G. H. Denton, J. G. Bockheim, S. C. Wilson, and A. R. Kerr (1994), Quaternary ice-level changes of upper Taylor Glacier, Antarctica: Implications for paleoclimate and ice-sheet dynamics, *Boreas*, 23, 29–43.
- McKelvey, B. (1981), The lithologic logs of DVDP cores 10 and 11, eastern Taylor Valley, in *Dry Valley Drilling Project, Antarct. Res. Ser.*, vol. 33, edited by L. D. McGinnis, pp. 63–94, AGU, Washington, D. C.
- McKelvey, B. (1982), Late Cenozoic marine and terrestrial glacial sedimentation in eastern Taylor Valley, Southern Victoria Land, *Antarctic Geoscience: Symposium on Antarctic Geology and Geophysics, Int. Union of Geol. Sci., Ser. B*, vol. 4, edited by C. Craddock et al., pp. 1109–1116, Univ. of Wis. Press, Madison.
- McKelvey, B., M. Hambrey, D. Harwood, M. Mabin, P. Webb, and J. Whitehead (2004), The Pagodroma Group—a Cenozoic record of the East Antarctic ice sheet in the northern Prince Charles Mountains, *Antarct. Sci.*, 13, 455–468.
- Monnin, E., et al. (2004), Evidence for substantial accumulation rate variability in Antarctica during the Holocene, through synchronization of CO<sub>2</sub> in the Taylor Dome, Dome C and DML ice cores, *Earth Planet. Sci. Lett.*, 224(1–2), 45–54, doi:10.1016/j.epsl.2004.05.007.
- Morse, D. L., E. D. Waddington, and E. J. Steig (1998), Ice age storm trajectories inferred from radar stratigraphy at Taylor Dome, Antarctica, *Geophys. Res. Lett.*, 25, 3383–3386.
- Morse, D. L., E. D. Waddington, H. P. Marshall, T. A. Neumann, E. J. Steig, J. E. Dibb, D. P. Winebrenner, and R. J. Arthern (1999), Accumulation rate measurements at Taylor Dome, East Antarctica: Techniques and Strategies for mass balance measurements in polar environments, *Geogr. Ann.*, Ser. A, 81, 683–694.
- Naish, T. (1997), Constraints on the amplitude of late Pliocene eustatic sea-level fluctuations: New evidence from the New Zealand shallow-marine sediment record, *Geology*, 25(12), 1139–1142.
- Naish, T., et al. (2005), An integrated sequence stratigraphic, palaeoenvironmental, and chronostratigraphic analysis of the Tangahoe Formation, southern Taranaki coast, with implications for mid-Pliocene (c. 3.4–3.0 Ma) glacio-eustatic sea-level changes, *J. R. Soc. N. Z.*, 35(1), 151–196.
- Naish, T., et al. (2009), Obliquity-paced Pliocene West Antarctic ice sheet oscillations, *Nature*, 458(7236), 322–328, doi:10.1038/nature07867.
- Oerlemans, J. (1997), Climate sensitivity of Franz-Josef Glacier, New Zealand, as revealed by numerical modelling, *Arct. Alp. Res.*, 29, 233–239.
- Orsi, A. H., and T. Whitworth (2004), *Hydrographic Atlas of the World Ocean Circulation Experiment (WOCE)*, vol. 1, *Southern Ocean*, edited by M. Sparrow et al., Int. WOCE Proj. Off., Southampton, U. K.
- Parizek, B. R., and R. B. Alley (2004), Ice thickness and isostatic imbalances in the Ross Embayment, West Antarctica: Model results, *Global Planet. Change*, 42(1–4), 265–278.
- Pattyn, F. (2006), GRANTISM: An Excel™ model for Greenland and Antarctic ice-sheet response to climate changes, *Comput. Geosci.*, 32, 316–325.
- Peltier, W. R. (2004), Global glacial isostasy and the surface of the ice-age earth: The ICE-5G (VM2) model and GRACE, *Annu. Rev. Earth Planet. Sci.*, 32, 111–149, doi:10.1146/annurev.earth.32.082503.144359.
- Piotrowski, J. A., N. K. Larsen, and F. W. Junge (2004), Reflections on soft subglacial beds as a mosaic of deforming and stable spots, *Quat. Sci. Rev.*, 23, 993–1000.
- Piotrowski, J. A., N. K. Larsen, J. Menzies, and W. Wysota (2006), Formation of subglacial till under transient bed conditions: deposition, deformation, and basal decoupling under a Weichselian ice sheet lobe, central Poland, *Sedimentology*, 53(1), 83–106, doi:10.1111/j.1365-3091.2005.00755.x.
- Pollard, D., and R. M. DeConto (2003), Antarctic ice and sediment flux in the Oligocene simulated by a climate-ice sheet-sediment model, *Palaeogeogr. Palaeoclimatol. Palaeoecol.*, 198(1–2), 53–67, doi:10.1016/S0031-0182(03)00394-8.
- Prentice, M. L., and A. G. Krusic (2005), Searly Pliocene Alpine glaciation in Antarctica: Terrestrial versus tidewater glaciers in Wright Valley, *Geogr. Ann.*, Ser. A, 87(1), 87–109.
- Pritchard, H. D., R. J. Arthern, D. G. Vaughan, and L. A. Edwards (2009), Extensive dynamic thinning on the margins of the Greenland and Antarctic ice sheets, *Nature*, 461(7266), 971–975, doi:10.1038/nature08471.
- Pyne, A. R., P. H. Robinson, and P. J. Barrett (1985), Core Log, Description, and Photographs: Ciros 2, Ferrar Fjord, Antarctica, *Antarct. Data Ser.*, vol. 11, 80 pp., Antarct. Res. Cent., Victoria Univ. of Wellington, Wellington, N. Z.
- Robinson, P. H. (1984), Ice dynamics and thermal regime of Taylor Glacier, South Victoria Land, Antarctica, *J. Glaciol.*, 30, 153–160.
- Shapiro, N., and M. Ritzwoller (2004), Inferring surface heat flux distributions guided by a global seismic model: Particular application to Antarctica, *Earth Planet. Sci. Lett.*, 223, 213–224.
- Siegert, M. J., P. Barrett, R. DeConto, R. Dunbar, C. Ó Cofaigh, S. Passchier, and T. Naish (2008), Recent advances in understanding Antarctic climate evolution, *Antarct. Sci.*, 20, 313–325.
- Staiger, J. W., D. R. Marchant, J. M. Schaefer, P. Oberholzer, J. V. Johnson, A. R. Lewis, and K. M. Swanger (2006), Plio-Pleistocene history of Ferrar Glacier, Antarctica: Implications for climate and ice sheet stability, *Earth Planet. Sci. Lett.*, 243(3–4), 489–503, doi:10.1016/j.epsl.2006.01.037.
- Steig, E. J., D. L. Morse, E. D. Waddington, M. Stuiver, P. M. Grootes, P. A. Mayewski, M. S. Twickler, and S. I. Whitlow (2000), Wisconsinan and Holocene climate history from an ice core at Taylor Dome, western Ross Embayment, Antarctica, *Geograf. Ann.*, Ser. A, 82, 213–235.
- Steig, E. J., D. P. Schneider, S. M. Rutherford, M. E. Mann, J. C. Comiso, and D. T. Shindell (2009), Warming of the Antarctic ice-sheet surface since the 1957 International Geophysical Year, *Nature*, 457, 459–462.
- Sugden, D. E., G. H. Denton, and D. R. Marchant (1993), The case for a stable East Antarctic ice sheet, *Geograf. Ann.*, Ser. A, 75, 151–151.
- Takeda, A., S. Cox, and A. J. Payne (2002), Parallel numerical modelling of the Antarctic Ice Sheet, *Comput. Geosci.*, 28(6), 723–734.
- Thorp, P. W. (1991), The glaciation and glacial deposits of the western Grampians, in *Glacial Deposits in Great Britain and Ireland*, edited by J. Ehlers, P. L. Gibbard, and J. Rose, pp. 137–149, Balkema, Rotterdam, Netherlands.
- van der Veen, C. J. (1999), *Fundamentals of Glacier Dynamics*, 462 pp., Balkema, Rotterdam, Netherlands.
- Vaughan, D. G., J. L. Bamber, M. Giovinetto, J. Russell, and A. P. R. Cooper (1999), Reassessment of net surface mass balance in Antarctica, *J. Clim.*, 12(4), 933–946.
- Vieli, A., and A. Payne (2003), Application of control methods for modelling the flow of Pine Island Glacier, West Antarctica, *Ann. Glaciol.*, 36(1), 197–204.
- Wardlaw, B., and T. Quinn (1991), The record of Pliocene sea-level change at Enewetak atoll, *Quat. Sci. Rev.*, 10(2–3), 247–258.
- Webb, P., and D. M. Harwood (1991), Late Cenozoic glacial history of the Ross embayment, Antarctica, *Quat. Sci. Rev.*, 10(2–3), 215–223, doi:10.1016/0277-3791(91)90020-U.
- Webb, P., D. Harwood, B. McKelvey, J. Mercer, and L. Stott (1984), Cenozoic marine sedimentation and ice-volume variation on the East Antarctic craton, *Geology*, 12(5), 287–291.
- Wilch, T., G. Denton, D. Lux, and W. McIntosh (1993), Limited Pliocene glacier extent and surface uplift in middle Taylor Valley, Antarctica, *Geograf. Ann.*, Ser. A, 75, 331–351.
- Wilson, G. S. (1995), The Neogene East Antarctic Ice-Sheet: A dynamic or stable feature?, *Quat. Sci. Rev.*, 14, 101–123.
- Winkelmann, R., M. A. Martin, M. Haseloff, T. Albrecht, E. Bueler, C. Khroulev, and A. Levermann (2010), The Potsdam Parallel Ice Sheet Model (PISM-PIK) – Part 1: Model description, *Cryosphere Discuss.*, 4, 1277–1306.
- Winter, D. (1995), Upper Neogene diatom biostratigraphy from coastal drillcores in Southern Victoria Land, Antarctica, M.S. thesis, 145 pp., Univ. of Nebr.-Lincoln, Lincoln.
- Winter, D., and D. Harwood (1997), Integrated diatom biostratigraphy of late Neogene drillholes in southern Victoria Land and correlation to Southern Ocean records, in *The Antarctic Region: Geological Evolution and Processes*, edited by C. Ricci, pp. 985–992, Terra Antart., Siena, Italy.
- Winter, D. M., C. Sjunneskog, and D. Harwood (2010), Early to mid-Pliocene environmentally constrained diatom assemblages from the AND-1B drillcore, McMurdo Sound, Antarctica, *Stratigraphy*, 7, 207–227.
- Winter, D., C. Sjunneskog, R. Scherer, P. Maffioli, C. Riesselman, and D. Harwood (2011), Pliocene-Pleistocene diatom biostratigraphy of near-shore Antarctica from the AND-1B drillcore, McMurdo Sound, *Global Planet. Change*, 16, in press.

N. R. Golledge, Antarctic Research Centre, Victoria University of Wellington, Kelburn Parade, Wellington 6140, New Zealand. (nick.golledge@vuw.ac.nz)

R. H. Levy, GNS Science, 1 Fairway Dr., Lower Hutt 5040, New Zealand.